A novel random chiral metamaterial with multi-step plateau for enhancing stiffness and energy absorption

Hao Wang[1], Mohammed Rafiq Abdul Kadir[2], Hanxing Zhu[3], Yongtao Lyu[1,4*]

[1]School of Mechanics and Aerospace Engineering, Dalian University of Technology, No. 2 Linggong Road, Dalian 116024, China

[2]Department of Biomedical Engineering, Faculty of Engineering, Universiti Malaya, 50603 Kuala Lumpur, Malaysia

[3]School of Engineering, Cardiff University, Queen's Building, the Parade, CF24 3AA, Cardiff, UK

[4]DUT-BSU Joint Institute, Dalian University of Technology, No. 2 Linggong Road, Dalian 116024, China

*Corresponding author

Dr. Yongtao Lyu,

School of Mechanics and Aerospace Engineering,

Dalian University of Technology,

No. 2 Lingong road,

Dalian 116024, China

Email: yongtaolu@dlut.edu.cn

Abstract

Chiral metamaterials are a class of auxetic mechanical metamaterials, which are widely employed for their remarkable auxetic behavior. However, they typically exhibit lower stiffness and energy absorption compared to other auxetic metamaterials at the same relative density. Therefore, enhancing the mechanical properties of chiral metamaterials through appropriate distribution of materials and geometric reconfigurations rather than simply adding more materials remains a significant challenge. In this study, a novel random structure called Vorochiral metamaterial was proposed by integrating Voronoi tessellation with conventional chiral metamaterials, effectively chiralizing the Voronoi structure. The mechanical properties of Vorochiral metamaterials, including Poisson's ratio, stiffness, energy absorption capacity, and deformation behaviors, were investigated through experimental testing and finite element (FE) analyses. The experimentally validated FE models were further used to investigate the mechanical properties of Vorochiral metamaterials with varying irregularity degrees and parametric analyses on the influence of nodal circle radius and wall thickness were conducted. The Vorochiral metamaterials demonstrated higher stiffness than conventional chiral metamaterials while maintaining a negative Poisson's ratio over a wide range of strains. Additionally, they exhibited superior energy absorption capacities due to multi-step plateaus in stress-strain curves. The results also showed that increasing the nodal circle radius decreased both stiffness and energy absorption capacity, whereas increasing the wall thickness enhanced both properties. These finding suggest that geometric reconfigurations can effectively enhance the mechanical properties of chiral metamaterials. This study successfully breaks the traditional trade-off between high stiffness and large deformability, demonstrating a significant improvement in mechanical performance compared to conventional chiral metamaterials.

Keywords: Voronoi tessellation; chiral metamaterial; chiralizing; negative Poisson's ratio; random structure; multi-step plateau

1 Introduction

Mechanical metamaterials are engineered structures with unprecedented mechanical properties governed by their microstructures rather than chemical compositions[1-8]. They are widely employed in aerospace, automotive, marine, and biomedical engineering. Their design typically relies on lattice or micro/nanostructures, enabling precise control over geometry and material distribution to achieve desired mechanical behaviors[9-15]. Auxetic mechanical metamaterials, also known as negative Poisson's ratio structures, exhibit counterintuitive deformation behavior – contracting laterally under compression and expanding laterally under tension[16-20]. Among them, chiral metamaterials represent a notable subclass, capable of maintaining a negative Poisson's ratio over a wide range of strains[21, 22]. They are highly regarded by researchers for their remarkable auxetic behavior. However, chiral metamaterials generally exhibit lower stiffness and energy absorption compared to other auxetic metamaterials at the same relative density. To enhance their stiffness, additional materials are often incorporated into the structure[23-25]. Although this method improves mechanical performance, it also increases both volume and mass. Therefore, a more efficient approach may be to enhance the mechanical properties through optimized material distribution and geometric reconfiguration, an area that remains a significant challenge.

Chiral structures are a class of negative Poisson's ratio metamaterials characterized by non-superimposable mirror images, providing mechanical stability under external loads[26-34]. Unlike re-entrant structures, which may lose their auxetic behavior due to instability at critical strain levels, chiral structures maintain both stability and auxeticity, making them less susceptible to failure. Prall and Lakes [35], building on Wojciechowski's theory [36], introduced a hexagonal honeycomb chiral structure whose unit cell consists of a central circular node with six ligaments symmetrically and rotationally connected around its axis. Additionally, anti-chiral structures feature adjacent nodes positioned on the same side of a shared ligament. In

chiral structures, the ligaments surrounding the nodes contract simultaneously under compression and expand under tension, resulting in a negative Poisson's ratio. Alderson et al. [37] found that incorporating cylinders at the nodes of chiral honeycomb structures reduced their stiffness compared to re-entrant hexagonal honeycomb structures. Furthermore, Alderson et al. [38] reported that anti-chiral honeycomb structures exhibited lower modulus values than chiral honeycomb structures with the same number of ligaments. To achieve periodicity in chiral structures, rotational symmetry constraints must be satisfied, allowing only five fundamental chiral configurations: trichiral, anti-trichiral, tetrachiral, anti-tetrachiral, and hexachiral. Gupta et al. [39] investigated the in-plane mechanical properties of trichiral and anti-trichiral structures, demonstrating that trichiral structures exhibited superior energy absorption capacity at equivalent relative densities. Meta-chiral structures, which do not adhere to rotational symmetry, integrate both chiral and anti-chiral elements to enhance auxeticity[40]. Grima et al. [40] combined tetrachiral and anti-tetrachiral structures to form a meta-chiral structure, modifying the nodes from cylindrical to rectangular, which resulted in a Poisson's ratio significantly lower than -1.0. Mizzi et al. [41] explored the mechanical properties and deformation behaviors of various chiral metamaterials derived from the chiralization of Euclidean tessellations. Geometric chiralization enables the development of novel chiral structures that may enhance mechanical properties while preserving negative Poisson's ratios. In essence, modifying the geometric distribution of conventional chiral metamaterials through tessellations can significantly improve their mechanical performance.

Voronoi tessellation, a widely used random pattern, mimics natural structures such as dragonfly wings, leaf veins, and nacreous formations[42-48]. Unlike conventional hexagonal honeycomb structures, Voronoi tessellations exhibit variability in both the number of edges per cell and the length of each edge[49-58]. As early as the late 20th century, Silva et al. [59, 60] conducted studies on the mechanical properties of 2D Voronoi tessellation honeycomb structures, including stiffness and strength. Their

research demonstrated that variations in the arrangements of honeycomb walls alter the overall elastic constants of the structure, and that non-periodic honeycombs exhibit greater strain under compression compared to periodic hexagonal honeycombs. Subsequently, Zhu et al. [61, 62] introduced the concept of the degree of regularity in Voronoi tessellation, which expands the design space. At lower relative densities, increased irregularity in Voronoi tessellation honeycombs was found to enhance both the dimensionless Young's modulus and shear modulus[61, 63, 64]. Zheng et al. [65] investigated the dynamic crushing performance of Voronoi tessellation honeycomb structures, showing that increased structural irregularity improves performance, including a higher plateau crush pressure compared to regular hexagonal honeycomb structures. Abdullahi and Gao [66] used a 2D Voronoi honeycomb-filled square tube structure to increase peak crushing force and specific absorption energy over regular square cell filling, thereby improving crashworthiness. Wang et al. [67] studied the mechanical properties of Voronoi honeycomb cylindrical shell structures and demonstrated that energy absorption capacity increases with decreasing irregularity. Overall, Voronoi tessellation structures exhibit superior stiffness and high energy absorption capacity compared to regular honeycomb structures. Therefore, integrating Voronoi tessellation into conventional designs presents a promising strategy for enhancing mechanical performance.

In this study, a novel metamaterial with a random structure, termed the "Vorochiral" metamaterial, was proposed by integrating Voronoi tessellation with chiral structures, effectively introducing chirality into the Voronoi-based architecture. This hybrid design combines the unique characteristics of both Voronoi tessellation and chiral metamaterials. The mechanical properties of Vorochiral metamaterials, including Poisson's ratio, stiffness, energy absorption capacity, and deformation behaviors, were investigated through experimental testing and finite element (FE) analyses. The experimentally validated FE models were further employed to examine the mechanical responses of Vorochiral metamaterials with varying degrees of irregularity. Additionally,

parametric studies were conducted to analyze on the effects of nodal circle radius and wall thickness. The results demonstrated that Vorochiral metamaterials exhibit a significant enhancement in mechanical performance compared to conventional trichiral metamaterials.

2 Methods

2.1 Generation of the geometric model

The proposed Vorochiral metamaterials were derived from the chiralization of Voronoi tessellation structures. The generation process of the Vorochiral diagram is illustrated in Fig. 1(a). The Voronoi tessellation diagram was generated using MATLAB (v2023b, MathWorks Inc., Massachusetts, USA) with 90 seed points (i.e., nuclei). Initially, the irregularity of the Voronoi tessellation was defined. To construct a regular hexagonal honeycomb with n cells in a square area A_0, the distance α_0 between any two adjacent nuclei should remain constant and is given by:

$$\alpha_0 = \sqrt{\frac{2A_0}{n\sqrt{3}}} \tag{1}$$

For a random Voronoi tessellation diagram with n cells in the square area A_0, the degree of irregularity Ir of Voronoi tessellation diagram can be defined as:

$$Ir = 1 - \frac{\alpha}{\alpha_0} \tag{2}$$

where α is the minimum distance between any two nuclei[61, 62]. For a regular hexagonal honeycomb, $\alpha = \alpha_0$ and $Ir = 0.0$, whereas, for a completely random (Poisson Voronoi) tessellation, $\alpha = 0.0$ and $Ir = 1.0$. In this study, n was set to 90, and A_0 was defined as a square area of 90 × 90 mm^2. Next, nodal circles with equal radii were placed at the vertices of the Voronoi tessellation and the tangentially-attached ligaments were connected to adjacent nodal circles. Each vertex was traversed using an adjacency matrix to generate chiral diagrams. If adjacent circles intersected or were tangent, no ligaments were created between them. For instance, as highlighted in the

dashed red box in Fig. 1(a), two trichiral diagrams were fused into a tetrachiral diagram. Therefore, the Vorochiral metamaterial can also be regarded as a combination of multiple types of chiral structures. The Vorochiral diagram was defined by assigning a radius R to the nodal circles. Finally, given a wall thickness t and an out-of-plane thickness T, the Vorochiral metamaterial was constructed using SolidWorks (v2023, SolidWorks Inc., Massachusetts, USA), as shown in Figs. 1(b)-1(g). Using this method, Vorochiral metamaterials with degrees of irregularity 0.0, 0.2, 0.4, 0.6, 0.8, and 1.0 were generated, as shown in Figs. 1(b)-1(g). Notably, when the degree of irregularity was 0.0, the Vorochiral metamaterial corresponded to a conventional trichiral metamaterial, as depicted in Fig. 1(b).

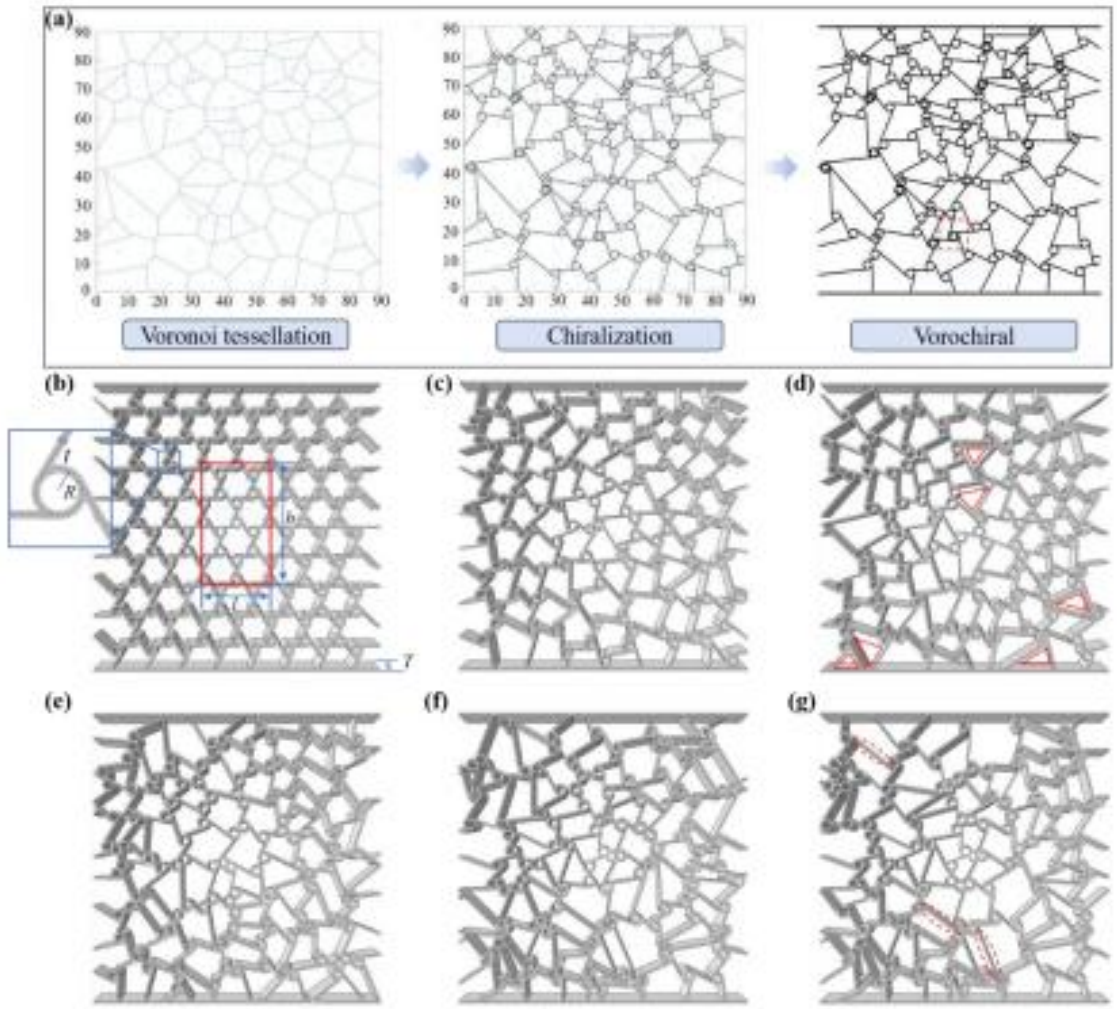

Figure 1 Vorochiral metamaterials. (a) The generation process of Vorochiral diagram. Vorochiral metamaterials with degrees of irregularity (b) 0.0, (c) 0.2, (d) 0.4, (e) 0.6, (f) 0.8, and (g) 1.0.

2.2 Experimental tests

2.2.1 Fabrication of specimens

The dumbbell-shaped standard specimens and Vorochiral metamaterials specimens were fabricated using the fused deposition modeling (FDM) method with a Bambu Lab P1S printer (Shenzhen, China), as shown in Fig. 2(a) and Fig. 3(a). The STL files, prepared using SolidWorks 2023, were imported into the Bambu Studio slicing software. A 0.4 mm nozzle was used for printing, with a set printing speed of 40.0 mm/s and a fixed layer height of 0.08 mm. Thermoplastic polyurethane (TPU) 95A HF, manufactured by Bambu Lab, was selected as the base material for specimen fabrication.

2.2.2 Material properties of TPU

The main material properties of TPU were obtained through uniaxial tensile tests. In accordance with the ASTM D638 international standard, dumbbell-shaped TPU specimens were modeled and fabricated. The geometry and dimensions of the standard specimen are presented in Fig. 2(a). Three specimens were tested using a universal testing machine (MTS Criterion 43.104) with a measuring range of 10.0 kN and a maximum force indicator error of less than $\pm 1.0\%$ at a constant testing speed of 10.0 mm/min, as shown in Fig. 2(b). The force-displacement data were recorded and used to calculate the nominal stress-strain curves. From the experimental data, a fitting curve for the hyperelastic material constitutive model was derived. Several hyperelastic constitutive models, including Mooney-Rivlin, Polynomial, Neo-Hookean, Arruda-Boyce, Yeoh, and Ogden, were evaluated against the average nominal stress-strain curve. Among them, the Polynomial ($N = 2$) model provided the best fit to the experimental results. The individual stress-strain curves obtained from the tensile tests are shown in Fig. 2(c). The resulting parameters of the Polynomial ($N = 2$) model were subsequently input into Abaqus (v2021, Dassault SIMULIA, Rhode Island, USA) to define the material properties, as summarized in Table 1.

Table 1 Material parameters of TPU

ρ (g/cm^3)	C_{10}	C_{01}	C_{20}	C_{02}	C_{11}	D_1	D_2
1.22	-8.95	15.95	0.10	3.30	-0.51	0.00	0.00

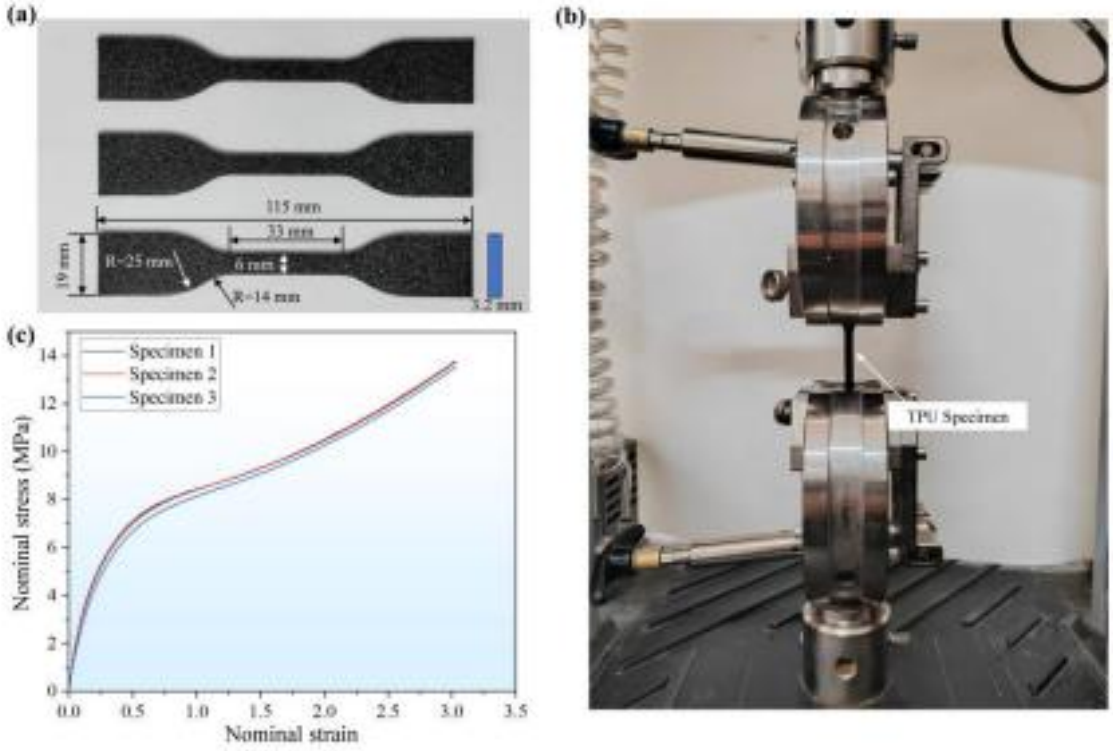

Figure 2 (a) Three TPU standard dumbbell-shaped tensile specimens and their dimensional parameters. (b) Experimental testing of dumbbell-shaped specimen. (c) Nominal stress-nominal strain curve of the base material.

2.2.3 Quasi-static compressive experimental tests

Quasi-static compressive tests of the Vorochiral metamaterials were conducted using the same MTS universal testing machine with a measuring range of 10.0 kN and a maximum force indicator error of less than $\pm$1.0% at a constant loading speed of 2.0 mm/min, as shown in Fig. 3(b). Each specimen was compressed to a displacement of 63.0 mm (corresponding to a strain of 0.7), and the resulting force-displacement curves were recorded. To capture the real-time deformation behavior, a high-resolution camera was positioned in front of the specimen during testing. A total of 18 specimens were tested, with three specimens prepared for each degree of irregularity, as shown in Fig.

3(a). All specimens had an out-of-plane thickness of 15.0 mm to prevent buckling or instability under compressive loads. Additionally, the relative density of each specimen was maintained at 20% to ensure consistency in material distribution and geometric comparisons.

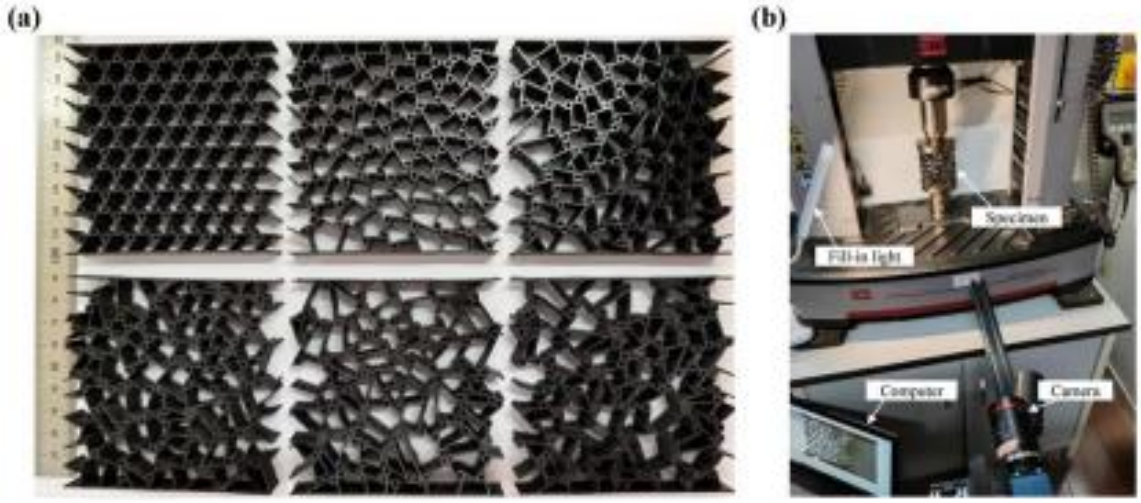

Figure 3 3D printing specimens and experimental testing platform. (a) The 3D printing specimens with varying degrees of irregularity. (b) Experimental testing platform used for quasi-static compressive tests.

2.3 FE analysis

The FE analysis in this study was performed using the commercial software Abaqus/Explicit 2021. Geometric models created in SolidWorks 2023 were imported into Abaqus, where the Polynomial (N = 2) material model was applied to simulate the mechanical behaviors of the Vorochiral metamaterials. Two rigid plates were positioned above and below the Vorochiral metamaterial, as shown in Fig. 4. The Vorochiral metamaterial was meshed using hexahedral solid elements (C3D8R), while the plates were meshed using quadrilateral shell elements (R3D4). A mesh sensitivity analysis was conducted to ensure mesh independence, revealing that a mesh size of 0.36 mm produced stable and converged simulation results. In the simulation setup, the bottom plate was fully constrained, and the top plate was displaced downward by 63.0 mm to compress the structure. The friction coefficient for tangential contact was 0.2, while the

normal contact behavior was modeled as "hard" contact. A force-displacement curve was obtained by extracting the reaction force and displacement at the node coupled to the top plate. From this data, the corresponding stress-strain curve was calculated to evaluate the mechanical response of the Vorochiral metamaterials.

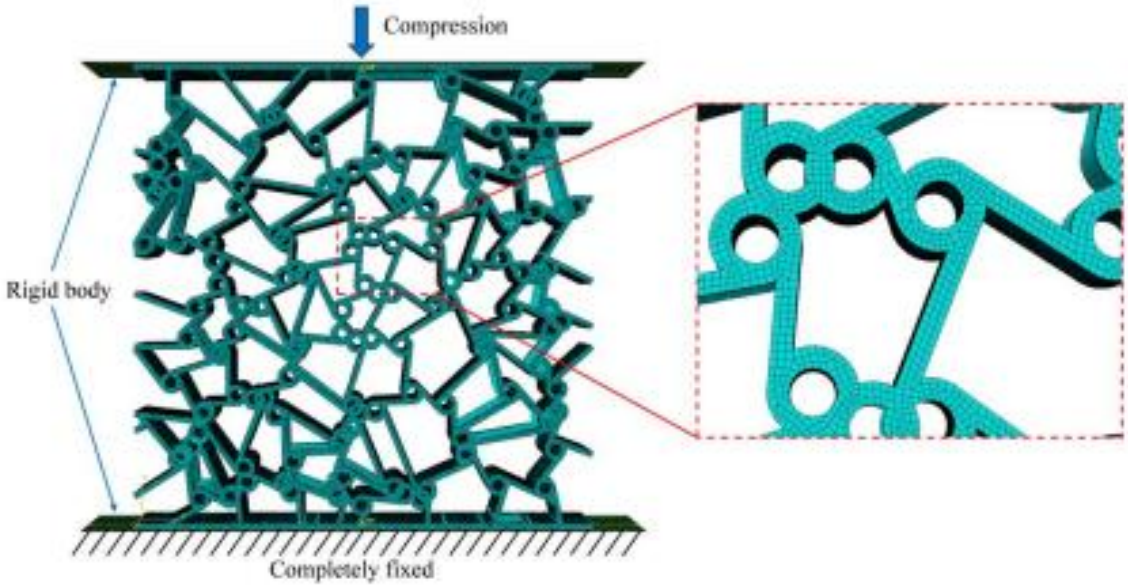

Figure 4 FE model of Vorochiral metamaterials.

2.4 Evaluation indicators of mechanical properties

The evaluation indicators of mechanical properties in this study were derived from the stress-strain curves of the Vorochiral metamaterials. Several key indicators were used to assess mechanical properties[68]: effective Poisson's ratio (v), apparent Young's modulus (E), energy absorption (EA), specific energy absorption (SEA), energy absorption efficiency (EAE), strain at the densification point (ε_d), and mean crushing load (MCL). Their definitions are as follows:

Poisson's ratio is a fundamental indicator of deformation behavior. To minimize boundary effects, the effective Poisson's ratio was calculated based on the interior region of the structure, specifically within the solid red box located at the center of the specimen[69], as shown in Fig. 1(b). The effective Poisson's ratio was determined by measuring and averaging the boundary displacements between the top and bottom edges, as well as the left and right sides of the solid red box during compression. The

effective Poisson's ratio (v) is given by:

$$v = -\frac{\varepsilon_x}{\varepsilon_y} \tag{3}$$

where ε_x and ε_y represent the nominal strains in the horizontal and vertical directions, respectively. The ε_x and ε_y are calculated using the following equation:

$$\varepsilon_x = \frac{\Delta\bar{x}}{l} \tag{4}$$

$$\varepsilon_y = \frac{\Delta\bar{y}}{h} \tag{5}$$

where l and h represent the initial horizontal and vertical lengths of the solid red box, respectively, as shown in Fig. 1(b). In this study, l was set to 20.0 mm, and h was set to 36.0 mm. $\Delta\bar{x}$ and $\Delta\bar{y}$ are the average deformation variations of the marked area in the horizontal and vertical directions, respectively.

Young's modulus is an indicator of stiffness, representing the ability to resist deformation. It is calculated from the linear elastic part of the stress-strain curve. The apparent Young's modulus (E) of the structure is calculated as below:

$$E = \frac{F/A}{\Delta h/H} \tag{6}$$

where F denotes the load carried by the structure under compression, H denotes the overall height of honeycomb, A and Δh are the surface area and displacement of upper boundary of the structure, respectively.

EA, SEA, EAE, ε_d, MCL are key indicators used to evaluate the energy absorption capacity of the Vorochiral metamaterials. EA in this study represents the cumulative energy absorption per unit volume, which can be obtained by integrating the stress-strain curve.

$$EA = \int_0^{\varepsilon_d} \sigma(\varepsilon)\mathrm{d}\varepsilon \tag{7}$$

SEA is the energy absorption of the structure per unit mass, which can be calculated as follow:

$$SEA = \frac{EA}{\rho_m \rho_v} \tag{8}$$

where ρ_m denotes the density of base material, and ρ_v denotes the relative density of

the undeformed structure. *EAE* is generally defined as the ratio of the actual energy output to the total input energy during the process of energy conversion or transfer for a system, which can be expressed as:

$$EAE = \frac{\int_0^{\varepsilon_a} \sigma(\varepsilon)\mathrm{d}\varepsilon}{\sigma_a} \tag{9}$$

where ε_a denotes the instantaneous strain that corresponds to the stress value σ_a. The strain at the densification point ε_d can be determined by the last local maximum value of *EAE*. The *MCL* represents the energy absorption per unit displacement, which can be calculated by:

$$MCL = \frac{\int_0^{d} F\mathrm{d}\delta}{d} \tag{10}$$

where *d* is the displacement corresponding to the ε_d.

3 Results and Discussion

3.1 Experimental validation

The FE models were validated against the experimental results, focusing on both the stress-strain curves and deformation behaviors. As illustrated in Fig. 5, the stress-strain curves from the FE simulations of Vorochiral metamaterials with varying degrees of irregularity closely followed the trends observed in the experimental results across all three specimens. However, due to minor discrepancies between the 3D-printed structures and the FE models, particularly in contact interactions, material parameters, and boundary conditions, the results from the FE simulation are slightly different from the experimental results. The *MCL* was used as a comparative indicator, and the errors among the three experimental tests and FEM were no more than 7.20% in varying configurations, as shown in Table 2. Additionally, as shown in Fig. 6, the deformation behaviors of Vorochiral metamaterials with different degrees of irregularity demonstrated a high degree of consistency between the experimental observations and simulation results.

Overall, the differences between the experimental data and FE simulation results remain within an acceptable range, thereby validating the accuracy and reliability of the FE models. Therefore, these validated models can be confidently employed in subsequent analyses to investigate the mechanical behavior of Vorochiral metamaterials.

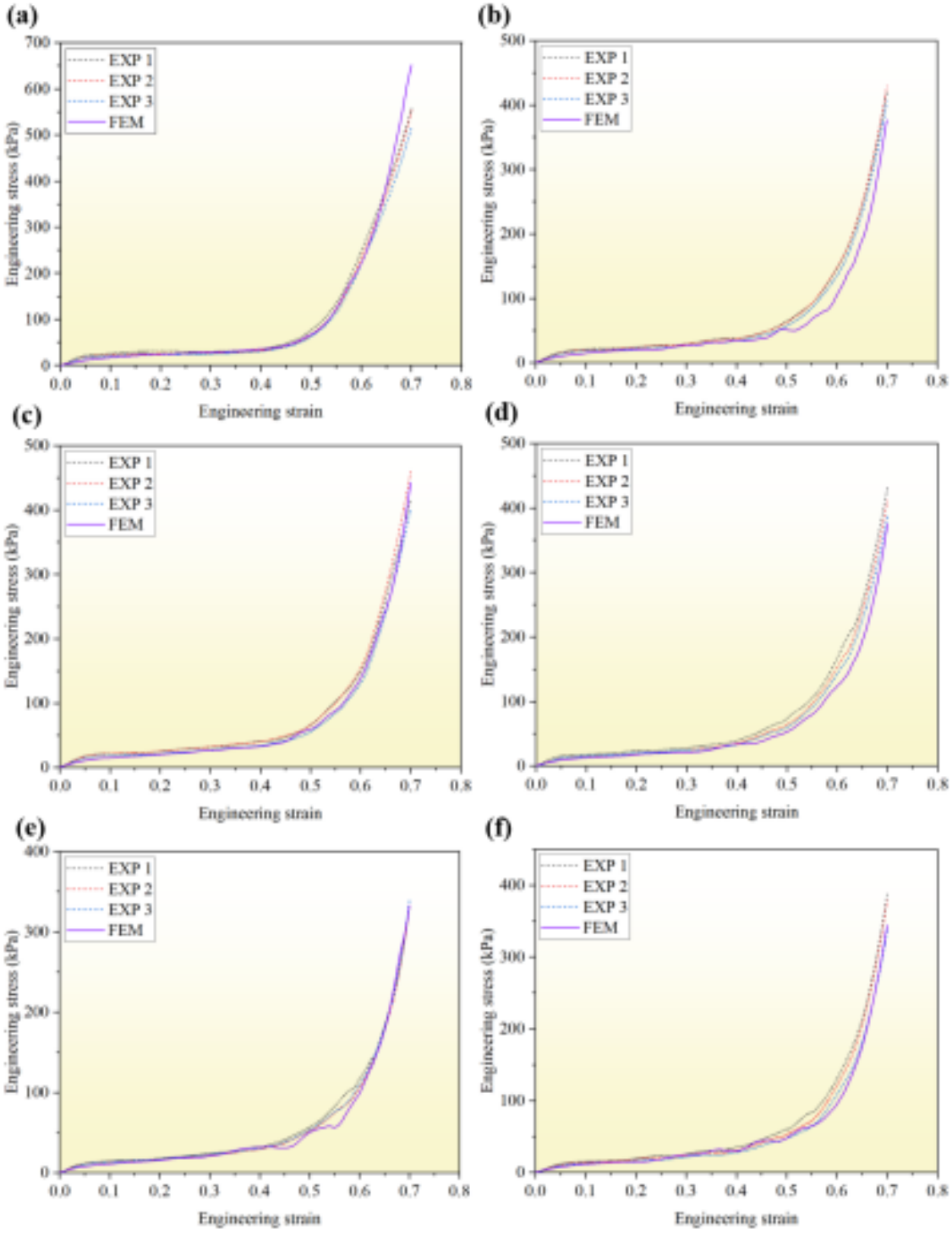

Figure 5 Comparison of stress-strain curves among three experimental tests and FEM. Irregularity degrees of (a) 0.0, (b) 0.2, (c) 0.4, (d) 0.6, (e) 0.8, and (f) 1.0.

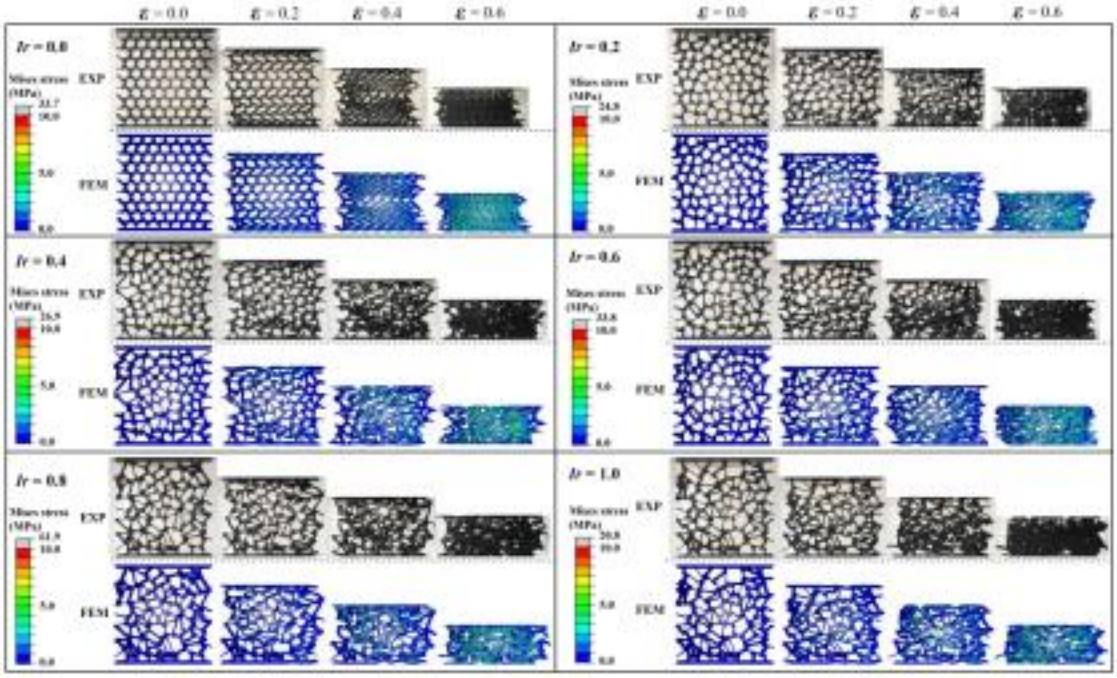

Figure 6 Comparison of deformation behaviors between experiment and FE with varying degrees of irregularity.

Table 2 *MCL* of Vorochiral metamaterials on three experimental tests and FEM

Ir	0.0	0.2	0.4	0.6	0.8	1.0
FEM	32.02	39.11	33.84	28.57	31.93	34.39
EXP 1	31.73	41.41	36.27	30.63	34.15	36.84
	(-0.92%)	(+5.88%)	(+7.17%)	(+7.20%)	(+6.97%)	(+7.11%)
EXP 2	32.49	40.62	34.82	30.13	32.94	32.63
	(+1.47%)	(+3.86%)	(+2.89%)	(+5.46%)	(+3.17%)	(-5.11%)
EXP 3	30.42	39.28	32.30	29.37	32.80	31.97
	(-4.99%)	(+0.42%)	(-4.54%)	(+2.80%)	(2.72%)	(-7.03%)

Note: "+" and "-" represent the enhancement and reduction compared to FEM, respectively.

3.2 Enhanced *E* and *EA* by chiralizing the Voronoi structure

Vorochiral metamaterial outperformed the conventional trichiral metamaterial in both *E* and *EA* by incorporating chirality into the Voronoi tessellation structure, while still retaining its auxetic effect. In this study, the concept of irregularity was introduced

to expand the design space and explore its influence on mechanical performance. To systematically investigate the effect of irregularity, the radius of the nodal circles and the relative density of all structures were fixed at 1.6 mm and 20%, respectively. The degree of irregularity was varied from 0.0 to 1.0 with an increment of 0.2.

As shown in Fig. 7(a), the effective Poisson's ratio of Vorochiral metamaterials with varying degrees of irregularity remained negative over a wide range of strains. These results confirm that a negative Poisson's ratio, the key characteristic of the chiral structure, successfully preserved in the proposed Vorochiral metamaterial design. Moreover, the strain range over which the negative Poisson's ratio was observed expanded to a broad range depending on the level of irregularity.

The Vorochiral metamaterials with lower degrees of irregularity exhibited higher apparent Young's moduli. To ensure the reliability of the results, six Vorochiral structures were randomly generated for each degree of irregularity and tested for their mechanical performance. As shown in Fig. 7(b), the apparent Young's modulus of Vorochiral metamaterials initially increased and then decreased with increasing irregularity. Among the tested configurations, the structures with an irregularity degree of 0.4 demonstrated the highest modulus. Moreover, Vorochiral metamaterials with irregularity degrees below 0.4 exhibited higher apparent Young's moduli than the conventional trichiral metamaterials (i.e., $Ir = 0.0$). Notably, the apparent Young's modulus of the Vorochiral metamaterial with an irregularity degree of 0.4 was enhanced by 13.88% compared to the conventional trichiral metamaterials, as presented in Table 3.

The Vorochiral metamaterials successfully retained a negative Poisson's ratio effect, inherent to chiral metamaterials. In other words, chiralizing Voronoi tessellations provides an effective approach for generating novel auxetic structures. The novel structures proposed in this study demonstrate the ability to simultaneously achieve higher stiffness and a negative Poisson's ratio – a combination that is difficult to realize. Moreover, the Vorochiral metamaterials exhibited a negative Poisson's ratio over a

broader range of strains compared to similar structures reported in previous studies[69], highlighting their enhanced mechanical performance and design potential.

The stiffness of the trichiral metamaterial can be enhanced by chiralizing the Voronoi tessellation structures. The Vorochiral metamaterials with lower degrees of irregularity exhibited higher stiffnesses, while those with higher irregularity showed a reduction in stiffness. This phenomenon can be attributed to the irregular ligament configurations formed at lower irregularities, particularly triangular arrangements within the internal structure, which provided additional support compared to conventional trichiral metamaterials, as shown in Fig. 1(d). However, as the degree of irregularity increased, excessively long ligaments may form, leading to localized reductions in stiffness, thereby diminishing the overall structural stiffness, as shown in Fig. 1(g). Stiffness reflects a material's ability to resist deformation, and structures with high deformability, such as conventional chiral and anti-chiral configurations, typically exhibit lower stiffness. Despite this, the Vorochiral metamaterials in this study were still able to maintain significant deformability, as shown in Fig. 7(a). Importantly, the geometric reconfiguration of chiral metamaterial using this approach effectively enhances stiffness, thereby breaking the conventional trade-off between high stiffness and large deformability.

The *EA* and *SEA* of the Vorochiral metamaterials, which represent their energy absorption capacity, were found to decrease with increasing irregularity, as shown in Fig. 7(c). Vorochiral structures with lower degrees of irregularity exhibited greater energy absorption capacity than the conventional trichiral metamaterials under the same relative density. Notably, the structure with an irregularity degree of 0.2 demonstrated a 63.04% improvement in energy absorption compared to the conventional trichiral configuration, as presented in Table 3. The strain at the densification point ε_d is a critical indicator of energy absorption and is defined as the strain corresponding to the last local maximum value of *EAE*, as shown in Fig. 8. The point marks the onset of the densification phase, where the integral of the stress-strain curve prior to ε_d

corresponds to the *EA*. The stress-strain curves of the Vorochiral metamaterials displayed a distinct multi-step plateau, indicating a unique energy absorption mechanism. For example, the stress-strain and *EAE* curves of Vorochiral metamaterial with structure configuration 4 of irregularity degree of 0.4 was depicted in detail in Fig. 9. The emergence of multi-step plateaus has enabled Vorochiral metamaterials to absorb energy in multiple stages, increasing the overall energy absorption capacity of the structure while also delaying the appearance of ε_d. Moreover, the *MCL* and ε_d jointly influence the overall energy absorption capacity, as higher *MCL* and ε_d are associated with improved energy absorption, as shown in Figs. 7(d) and 7(e). Furthermore, Fig. 7(f) presents a radar diagram offering a comprehensive visualization of the mechanical performance of Vorochiral metamaterials across different degrees of irregularity. A larger enclosed area in the radar plot indicates superior overall performance. Especially, structures with irregularity degrees of 0.2 and 0.4 exhibit significantly enhanced mechanical properties compared to other configurations.

The energy absorption capacity of trichiral metamaterials can also be enhanced by chiralizing Voronoi tessellation structures. As the degree of irregularity increased, the energy absorption capacity of the Vorochiral metamaterials decreased, consistent with trends observed in conventional Voronoi honeycombs[64]. The superior energy absorption observed in Vorochiral metamaterials with lower irregularity, compared to the conventional trichiral structure, can be mainly attributed to the occurrence of multi-step plateaus in the stress-strain curves of Vorochiral metamaterials. The structures with multi-step plateaus have strong energy absorption capacity, which were reported in many previous studies[70-78]. The occurrence of these multi-step plateaus was likely attributed to multiple self-contact interactions within the structure during compression, which momentarily altered the deformation pathway, as shown in Fig. 9. The places of self-contact for each stage were marked with red ovals. The places of self-contact increased gradually with the compression of the structure. Each increase in the number of self-contact places also significantly increased the stress on the entire structure

during compression, forming each local maximum value of *EAE*. In contrast, the trichiral metamaterial had only one maximum value in the *EAE* curve, which meant that all self-contacts occur almost simultaneously when the structure was compressed. Thus, the trichiral metamaterial also had only one plateau stage in the stress-strain curve. Additionally, higher *MCL* and larger ε_d can led to a stronger energy absorption capacity. Therefore, Vorochiral metamaterials with higher degrees of irregularity exhibited a notable decrease in *MCL*, which contributed to the overall reduction in energy absorption capacity.

Table 3 *E*, *EA* and *SEA* of Vorochiral metamaterials

Ir	*E* (kPa)	*EA* (kJ/m^3)	*SEA* (J/kg)
0.0	272.97±0.00	10.12±0.00	41.48±0.00
0.2	279.87±23.99 (+2.5%)	16.50±0.93 (+63.04%)	67.62±3.80 (+63.04%)
0.4	310.85±33.12 (+13.88%)	13.51±2.27 (+33.50%)	55.35±9.30 (+33.50%)
0.6	267.78±27.32 (-1.90%)	12.55±1.46 (+24.01%)	51.43±5.97 (+24.01%)
0.8	242.71±23.24 (-11.08%)	12.29±2.36 (+21.44%)	50.39±9.69 (+21.44%)
1.0	221.27±27.43 (-18.94%)	11.45±2.09 (+13.14%)	46.94±8.56 (+13.14%)

Note: "+" and "-" represent the enhancement and reduction compared to "*Ir* = 0.0", respectively.

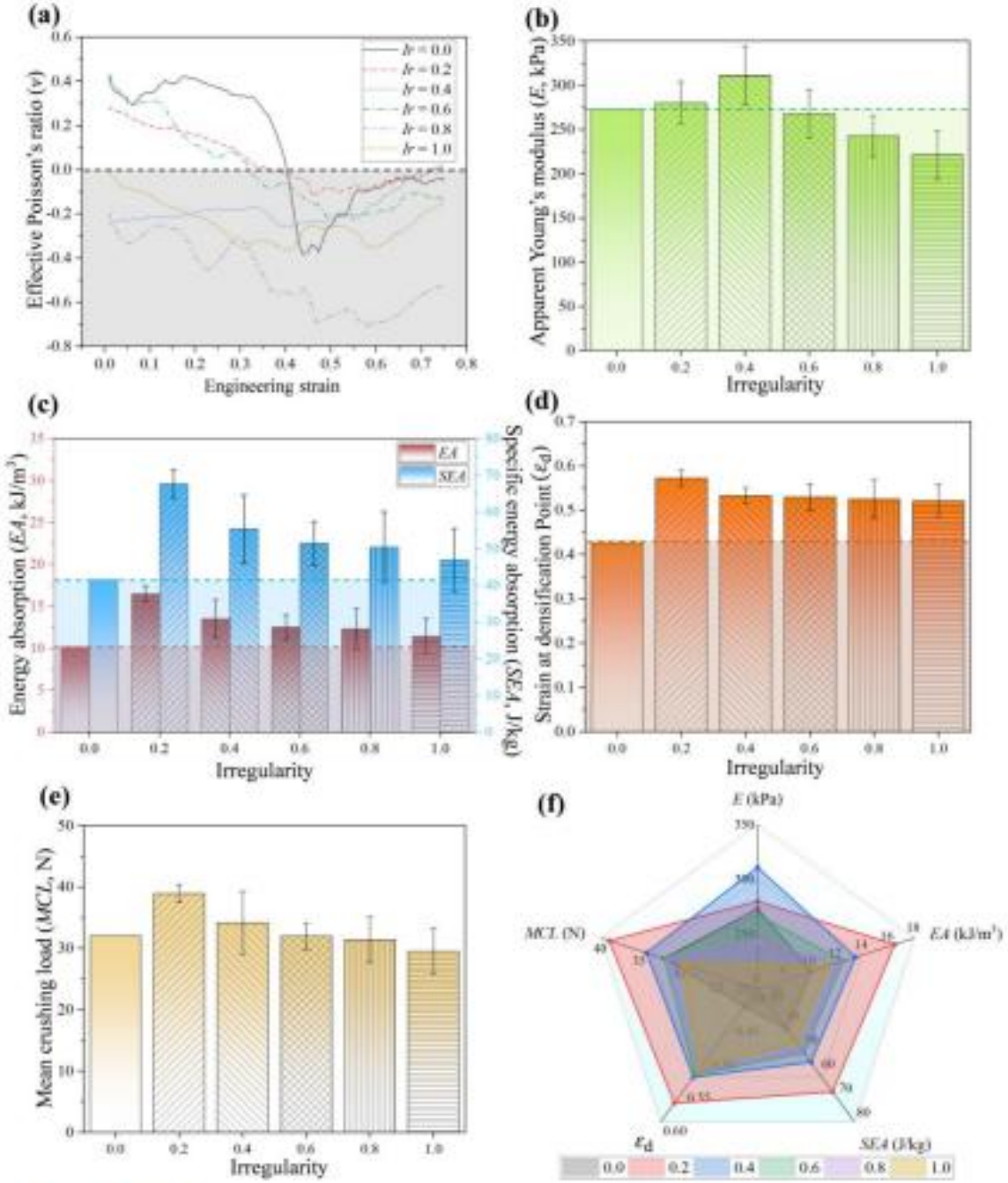

Figure 7 Mechanical indicators of Vorochiral metamaterials with varying degrees of irregularity (Ir). (a) Effective Poisson's ratio (v) of Vorochiral metamaterials with different degrees of irregularity. (b) Apparent Young's modulus (E), (c) energy absorption (EA), specific energy absorption (SEA), (d) strain at densification point (ε_d), and (e) mean crushing load (MCL) of Vorochiral metamaterials with different degrees of irregularity. (f) Radar diagram of various indicators of Vorochiral metamaterials with different degrees of irregularity.

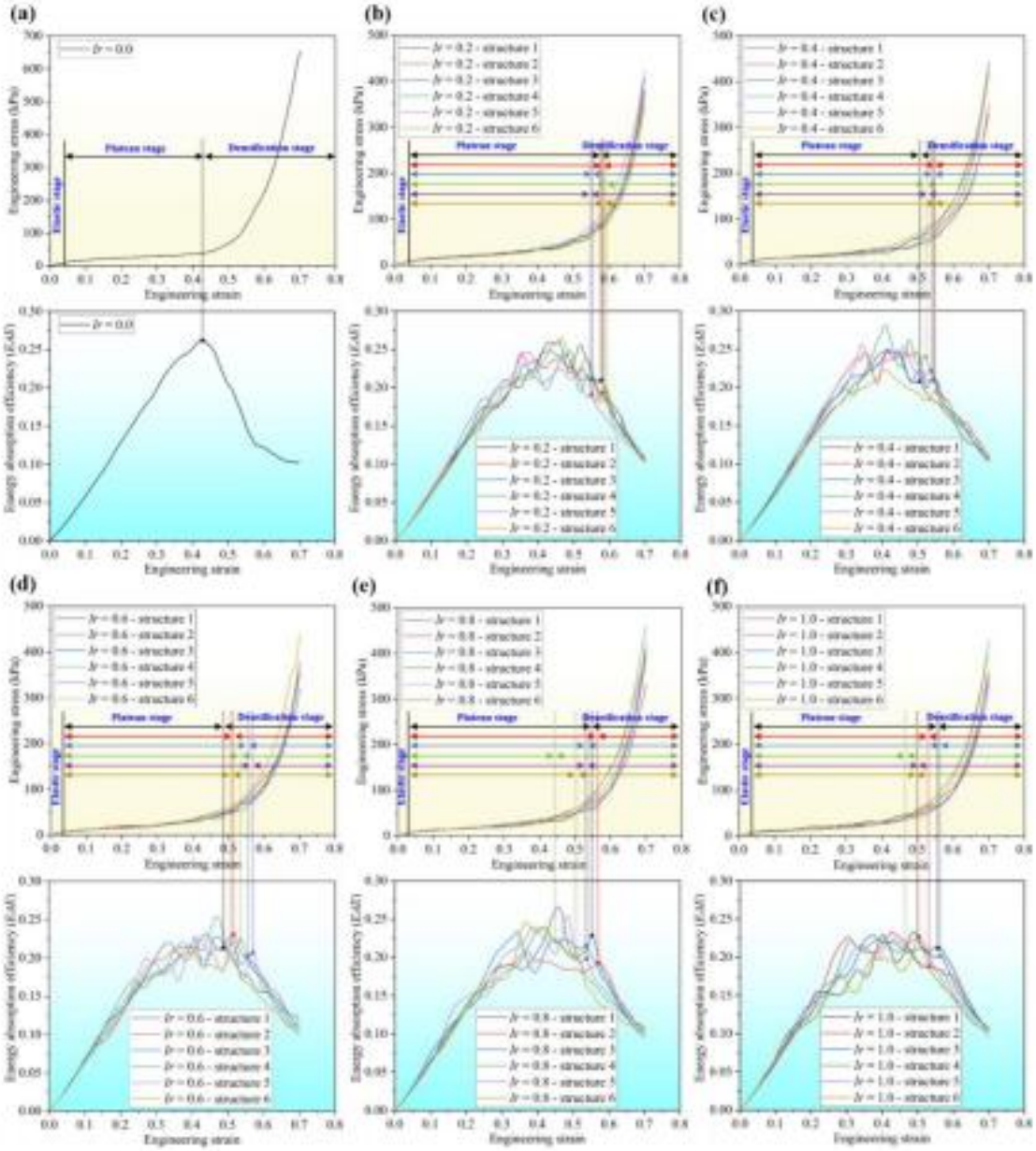

Figure 8 Stress-strain curves and energy absorption efficiency (*EAE*) curves of Vorochiral metamaterials with degrees of irregularity (*Ir*) (a) 0.0, (b) 0.2, (c) 0.4, (d) 0.6, (e) 0.8, and (f) 1.0. The stars with different colors represent the last local maximum values of *EAE* curves, respectively.

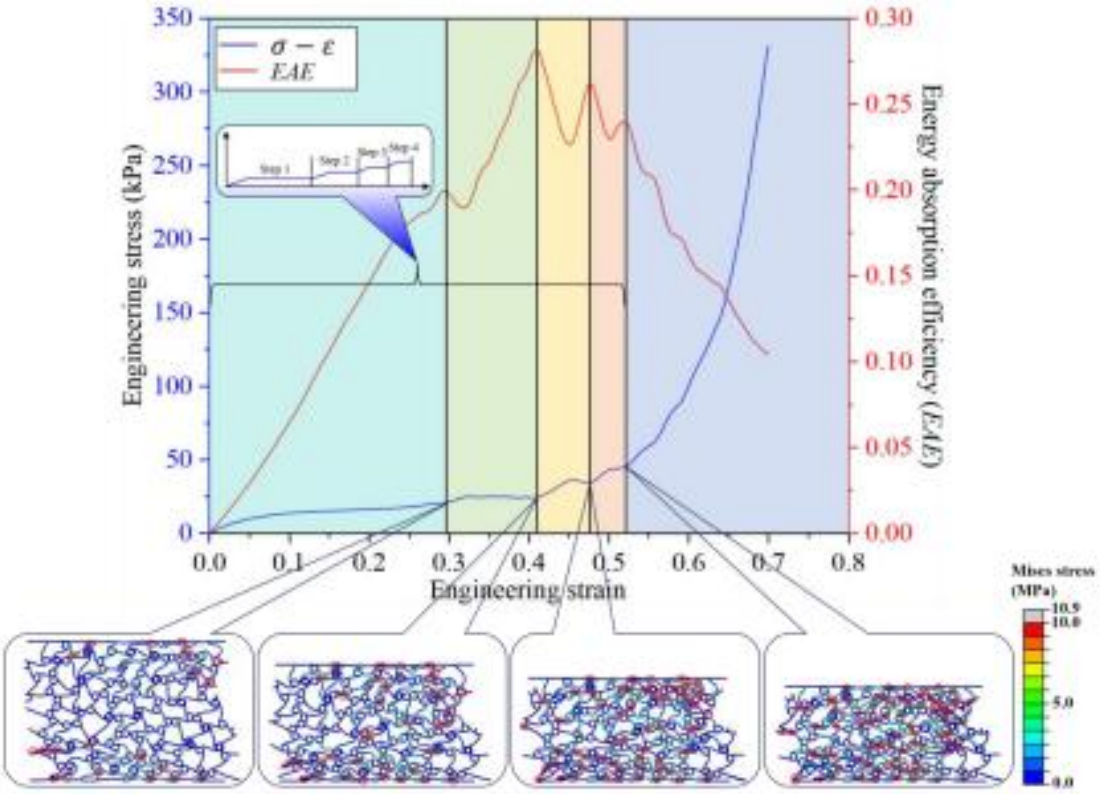

Figure 9 Stress-strain curve of '*Ir* = 0.4 – structure 4' with a multi-step plateau, energy absorption efficiency (*EAE*) curve, and deformation modes with self-contact interactions. The places of self-contact for each stage are marked with red ovals.

3.3 Parametric studies

3.3.1 Effect of nodal circle radius

The radius of the nodal circles in Vorochiral metamaterials plays a crucial role in influencing the mechanical properties of the structures. To investigate this effect, the degree of irregularity and the relative density of all configurations were fixed at 1.0 and 20%, respectively. The radii of the nodal circles were varied from 1.0 mm to 2.0 mm, with an interval of 0.2 mm. The deformation behavior of Vorochiral metamaterials with varying nodal circle radii under compression is shown in Fig. 10. While the general deformation pattern remained similar across all configurations, an increase in nodal circles radius led to a decrease in the apparent Young's modulus of the Vorochiral metamaterials, as shown in Fig. 11(a). Both the *EA* and *SEA* generally decreased with

increasing radius, as illustrated in Fig. 11(b). Similarly, the ε_d of varying configurations decreased as increasing radius, as presented in Fig. 11(c) and 11(d). Additionally, the *MCL* across these configurations also exhibited an overall decreasing trend as the radius of the nodal circles increased, as shown in Fig. 11(e).

The stiffness of the Vorochiral metamaterials was observed to decrease with increasing nodal circle radius. As the radius increased, the circumference of each nodal circle became longer, resulting in a reduction in wall thickness to maintain a constant overall relative density. This decrease in wall thickness is likely the primary factor contributing to the reduction in the stiffness of the structures.

The energy absorption capacity of the Vorochiral metamaterials decreased with increasing radius of the nodal circles. As shown in Figs. 11(c)-11(e), the ε_d values and the *MCL* exhibited a gradual decline with increasing radius. This trend explains the overall reduction in energy absorption capacity as the nodal circle radius increased.

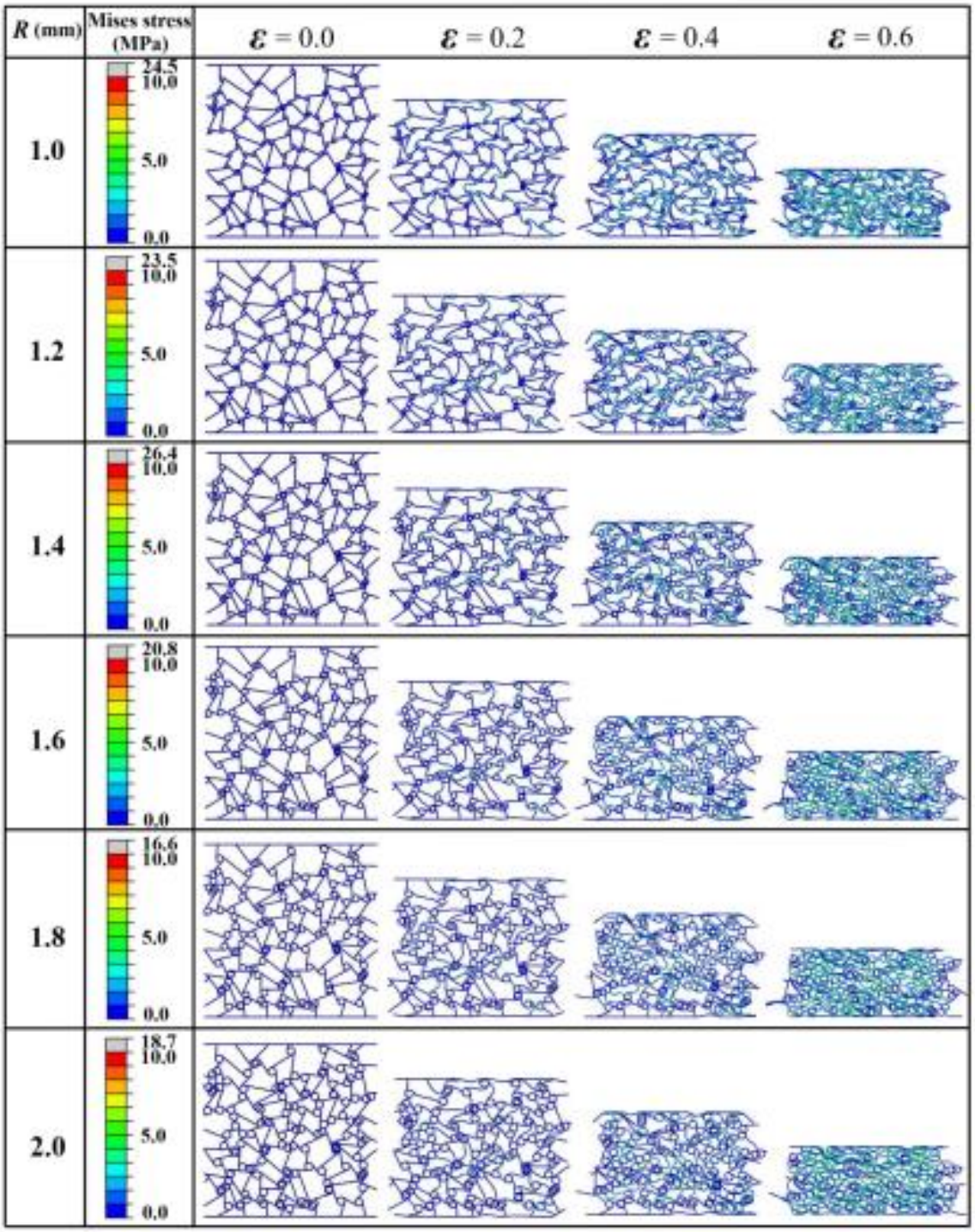

Figure 10 Deformation behaviors of Vorochiral metamaterials with varying radii of nodal circles.

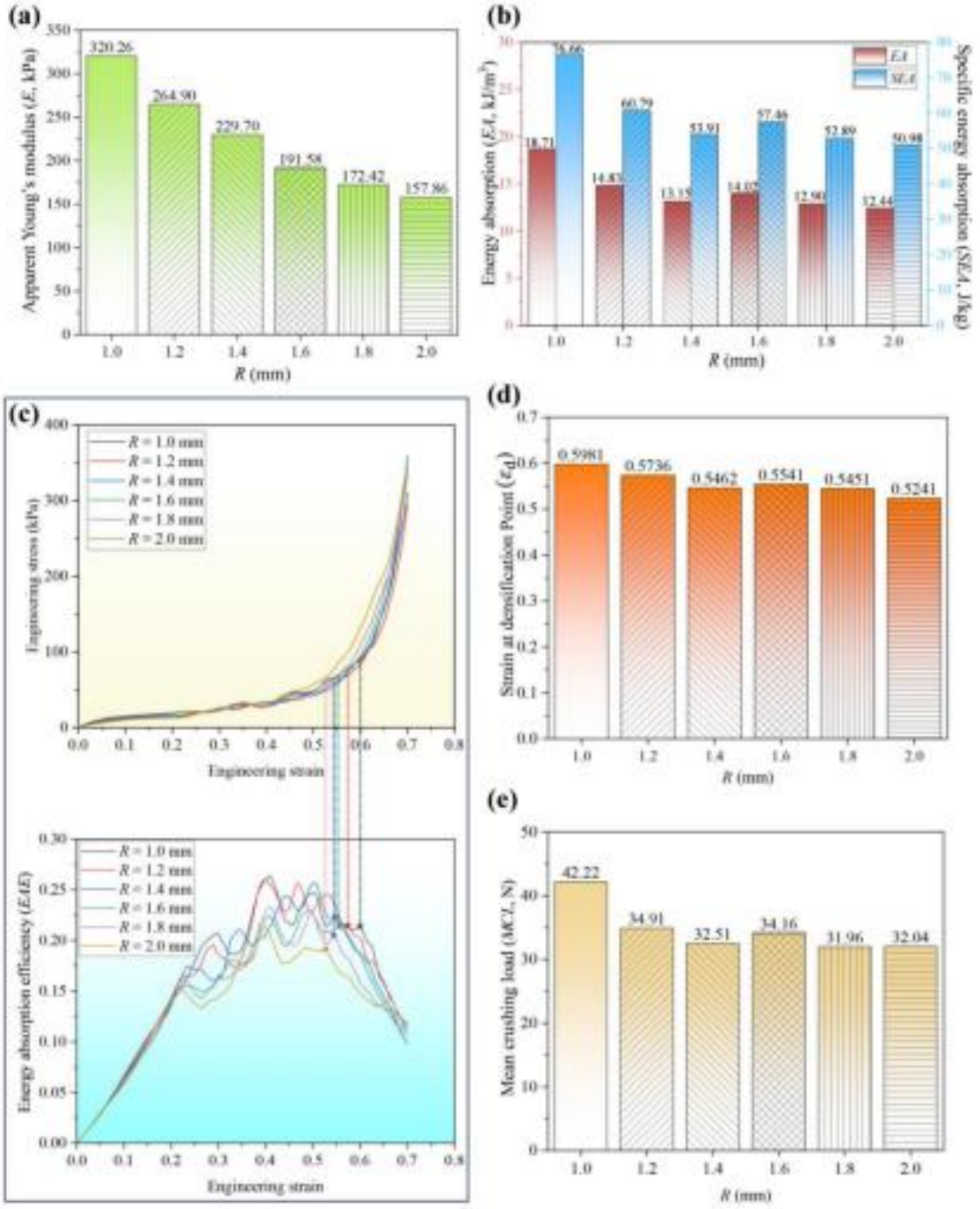

Figure 11 Mechanical indicators of Vorochiral metamaterials with varying radii of nodal circles. (a) Apparent Young's modulus (E) of Vorochiral metamaterials. (b) Energy absorption (EA) and specific energy absorption (SEA) of Vorochiral metamaterials. (c) Stress-strain curve and energy absorption efficiency (EAE) of Vorochiral metamaterials. The stars with different colors represent the last local maximum values of EAE curves, respectively. (d) Strain at densification point (ε_d) of Vorochiral metamaterials. (e) Mean crushing load (MCL) of Vorochiral metamaterials.

3.3.2 Effect of wall thickness

The wall thickness of the Vorochiral metamaterials directly influenced the relative density of the structures. To examine its effect, the degree of irregularity and the radius of the nodal circles were fixed at 1.0 and 1.6 mm, respectively. The wall thickness was varied from 0.5 mm to 1.0 mm in increments of 0.1 mm. The deformation process of Vorochiral metamaterials with varying wall thickness is illustrated in Fig. 12. While the overall deformation behaviors remained similar across configurations, local stress concentrations increased with wall thickness under the same compressive strain levels. As shown in Fig. 13(a), the apparent Young's modulus of the Vorochiral metamaterials increased significantly with thicker walls, indicating improved stiffness. Similarly, both the *EA* and *SEA* increased with wall thickness, as shown in Fig. 13(b). Although the ε_d decreased as wall thickness increased, the stress values at equivalent strain levels rose markedly, as illustrated in Fig. 13(c) and 13(d). Furthermore, the *MCL* exhibited substantial improvement with increasing wall thickness, as depicted in Fig. 13(e).

The stiffness of the Vorochiral metamaterials was significantly enhanced with increasing wall thickness, indicating that wall thickness is one of the most crucial factors in determining the structural stiffness. Once the geometric configuration of the structure is defined, the relative density (i.e., solid volume fraction) is governed solely by the wall thickness.

Similarly, the energy absorption capacity of the Vorochiral metamaterials also increased with wall thickness. As shown in Figs. 12(c)-12(e), variations in the *MCL* had a more pronounced effect on the energy absorption capacity than the changes in ε_d, contributing to the improvement of energy absorption capability.

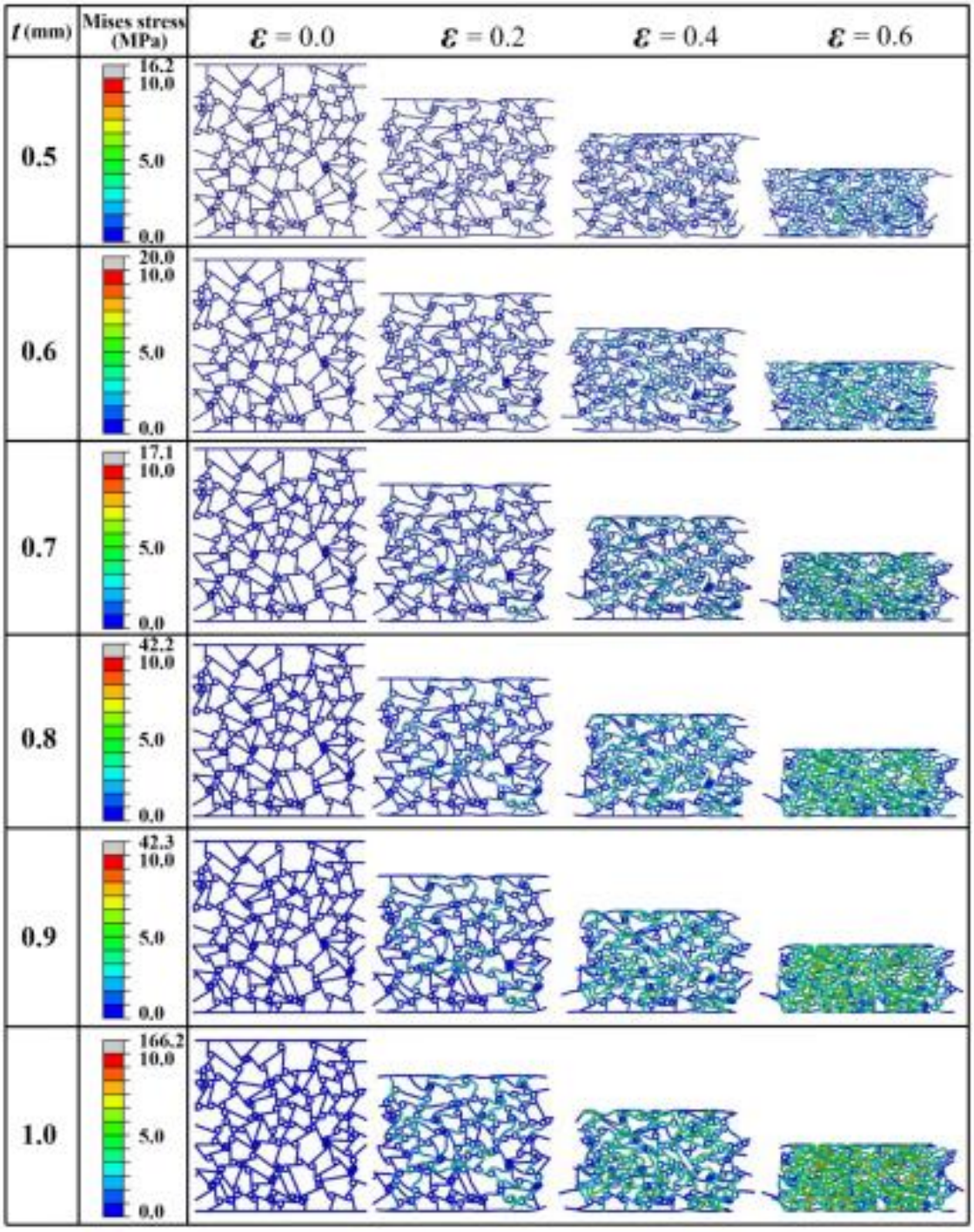

Figure 12 Deformation behaviors of Vorochiral metamaterials with varying thicknesses of wall.

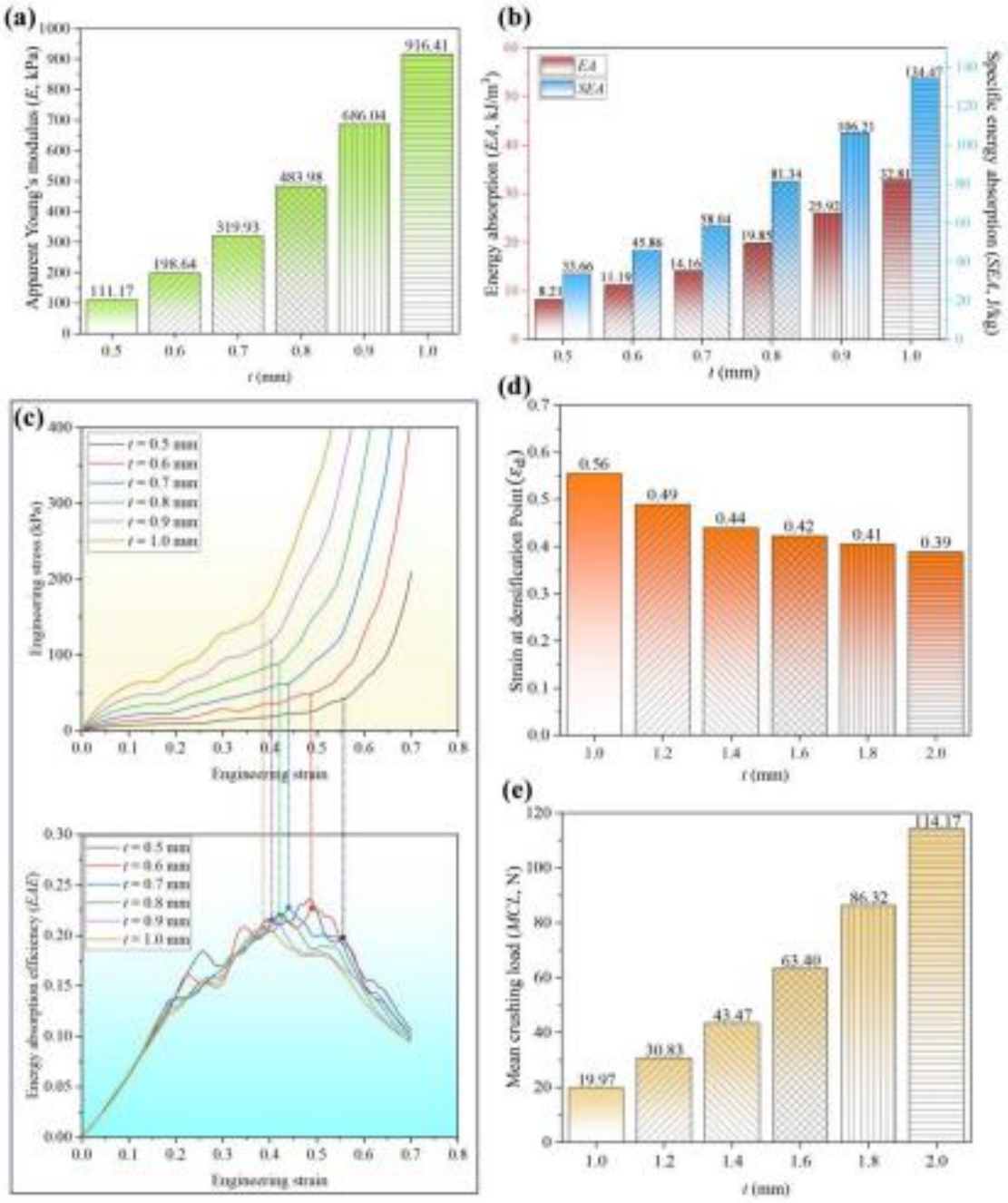

Figure 13 Mechanical indicators of Vorochiral metamaterials with varying thicknesses of wall. (a) Apparent Young's modulus (E) of Vorochiral metamaterials. (b) Energy absorption (EA) and specific energy absorption (SEA) of Vorochiral metamaterials. (c) Stress-strain curve and energy absorption efficiency (EAE) of Vorochiral metamaterials. The stars with different colors represent the last local maximum values of EAE curves, respectively. (d) Strain at densification point (ε_d) of Vorochiral metamaterials. (e) Mean crushing load (MCL) of Vorochiral metamaterials.

Although the mechanical properties of the Vorochiral metamaterials were superior to those of conventional trichiral metamaterials, several limitations remain in this study. First, while the Vorochiral metamaterials retained the key characteristic of a negative Poisson's ratio over a wide range of strains, the Poisson's ratio could not be arbitrarily controlled. Further studies should explore the design of Vorochiral metamaterials with customizable Poisson's ratio to enable broader functional applications. Second, due to the influence of boundary effects, it was challenging for the overall structure to consistently exhibit a pronounced negative Poisson's ratio. The application of appropriate boundary conditions remains a complex issue. In particular, the periodic boundary conditions commonly used for unit cells of periodic structures were not directly applicable in this study. Therefore, further research is needed to develop and implement suitable boundary conditions for these types of non-periodic structures. Third, the number of nuclei used in generating the Vorochiral metamaterials was not varied in this study. Modifying the number and distribution of nuclei could provide valuable insights into how these parameters affect the mechanical performance of Vorochiral metamaterials and should be considered in future investigations.

4 Conclusions

In this study, a novel random structure termed the Vorochiral metamaterial was proposed by chiralizing the Voronoi tessellation structure. The Poisson's ratio, stiffness, energy absorption capacity, and deformation behaviors of the Vorochiral metamaterials were systematically investigated. Moreover, the experimentally validated FE models were employed to examine the mechanical performance of Vorochiral metamaterials with varying degrees of irregularity, along with parametric studies on nodal circle radius and wall thickness. The key conclusions drawn from the present study are as follows:

(1) The negative Poisson's ratio effect was expanded to a wider range of strain in Vorochiral metamaterials with varying degrees of irregularity.

(2) Vorochiral metamaterials with lower degrees of irregularity significantly

outperformed conventional trichiral metamaterials in stiffness and energy absorption capacity.

(3) The multi-step plateaus in stress-strain curves contributed to improved energy absorption capacity, when Vorochiral metamaterials were compressed.

(4) For fixed degree of irregularity and relative density, both stiffness and energy absorption capacity exhibited an overall decreasing trend as the radius of the nodal circles increased.

(5) For fixed degree of irregularity and nodal circle radius, increasing the wall thickness significantly enhanced both stiffness and energy absorption capacity.

Overall, excellent mechanical performance of the Vorochiral metamaterials was achieved by integrating Voronoi tessellation structures with chiral metamaterials. This geometric reconfiguration approach effectively enhanced key mechanical properties, breaking the traditional trade-off between high stiffness and large deformability. Additionally, due to the occurrence of multi-step plateau in stress-strain curves, the energy absorption capacity of the Vorochiral metamaterials was also significantly enhanced compared to that of conventional trichiral metamaterial. These advancements highlight the potential of Vorochiral metamaterials for high performance applications across various engineering fields, including aerospace, automotive, marine, and biomedical engineering.

CRediT authorship contribution statement

Hao Wang: Conceptualization, Methodology, Software, Writing – Original draft. **Mohammed Rafiq Abdul Kadir:** Writing – review & editing, Validation, Supervision. **Hanxing Zhu:** Writing – review & editing, Investigation, Supervision. **Yongtao Lyu:** Writing – review & editing, Conceptualization, Funding acquisition, Project administration.

Declaration of competing interest

The authors declare that they have no known competing financial interests or personal relationships that could have appeared to influence the work reported in this

paper.

Data availability

The data supporting the numerical results in this study is available from the authors upon reasonable request.

Acknowledgements

This work was supported by the National Key R&D Program of China (grant number 2024YFE0213500), National Natural Science Foundation of China (grant number 12072066), and the Fundamental Research Funds for the Central Universities (grant number DUTIO-ZG-202501). Thanks to Prof. Stephen Richmond from Cardiff University for proofreading this manuscript.

References

[1] Jiao P, Mueller J, Raney JR, Zheng X, Alavi AH. Mechanical metamaterials and beyond. Nat. Commun. 2023; 14: 6004.

[2] Ma WWS, Yang H, Zhao Y, et al. Multi-physical lattice metamaterials enabled by additive manufacturing: design principles, interaction mechanisms, and multifunctional applications. Adv. Sci. 2025; 12 (8): 2405835.

[3] Wang H, Lyu Y, Bosiakov S, Zhu H, Ren Y. A review on the mechanical metamaterials and their applications in the field of biomedical engineering. Front. Mater. 2023; 10: 1273961.

[4] Bertoldi K, Vitelli V, Christensen J, van Hecke M. Flexible mechanical metamaterials. Nat. Rev. Mater. 2017; 2 (11): 17066.

[5] Zadpoor, Amir, A. Mechanical meta-materials. Mater. Horiz. 2016; 3 (5): 371-81.

[6] Sinha P, Mukhopadhyay T. Programmable multi-physical mechanics of mechanical metamaterials. Mater. Sci. Eng., R 2023; 155: 100745.

[7] Pishvar M, Harne RL. Foundations for soft, smart matter by active mechanical metamaterials. Adv. Sci. 2020; 7 (18): 2001384.

[8] Khalid MY, Arif ZU, Tariq A, Hossain M, Umer R, Bodaghi M. 3d printing of

active mechanical metamaterials: a critical review. Mater. Des. 2024; 246: 113305.

[9] Craster R, Guenneau S, Kadic M, Wegener M. Mechanical metamaterials. Rep. Prog. Phys. 2023; 86 (9): 94501.

[10] Yu X, Zhou J, Liang H, Jiang Z, Wu L. Mechanical metamaterials associated with stiffness, rigidity and compressibility: a brief review. Prog. Mater. Sci. 2018; 94: 114-73.

[11] Lee JH, Singer JP, Thomas EL. Micro-/nanostructured mechanical metamaterials. Adv. Mater. 2012; 24 (36): 4782-810.

[12] Qi J, Chen Z, Jiang P, et al. Recent progress in active mechanical metamaterials and construction principles. Adv. Sci. 2022; 9 (1): e2102662.

[13] Zaiser M, Zapperi S. Disordered mechanical metamaterials. Nat. Rev. Phys. 2023; 5 (11): 679-88.

[14] Chen Y, Mai Y, Ye L. Perspectives for multiphase mechanical metamaterials. Mater. Sci. Eng., R 2023; 153: 100725.

[15] Kadic M, Milton GW, van Hecke M, Wegener M. 3d metamaterials. Nat. Rev. Phys. 2019; 1: 198-210.

[16] Kolken HMA, Zadpoor AA. Auxetic mechanical metamaterials. RSC Adv. 2017; 7 (9): 5111-29.

[17] Lu C, Hsieh M, Huang Z, et al. Architectural design and additive manufacturing of mechanical metamaterials: a review. Engineering 2022; 17: 44-63.

[18] Gu J, Zhao W, Zeng C, Liu L, Leng J, Liu Y. Construction of mechanical metamaterials and their extraordinary functions. Compos. Struct. 2025; 356: 118872.

[19] Grima JN, Gatt R. Perforated sheets exhibiting negative poisson's ratios. Adv. Eng. Mater. 2010; 12 (6): 460-4.

[20] Veerabagu U, Palza H, Quero F. Review: auxetic polymer-based mechanical metamaterials for biomedical applications. ACS Biomater. Sci. Eng. 2022; 8 (7): 2798-824.

[21] Wu W, Hu W, Qian G, Liao H, Xu X, Berto F. Mechanical design and multifunctional applications of chiral mechanical metamaterials: a review. Mater. Des. 2019; 180: 107950.

[22] Yuan X, Chen M, Yao Y, et al. Recent progress in the design and fabrication of multifunctional structures based on metamaterials. Curr. Opin. Solid State Mater. Sci. 2021; 25 (1): 100883.

[23] Yong J, Li W, Dong Y, et al. Dual characteristics of static stiffness and adjustable bandgap of innovative re-entrant hybrid chiral metamaterials. Thin-Walled Struct. 2024; 203: 112168.

[24] Hou R, Dong P, Hu J, et al. An optimized lozenge-chiral auxetic metamaterial with tunable auxeticity and stiffness. Mater. Des. 2024; 237: 112530.

[25] Frenzel T, Hahn V, Ziemke P, et al. Large characteristic lengths in 3d chiral elastic metamaterials. Commun. Mater. 2021; 2: 4.

[26] Gupta A, Sharma S, Madke RR, Chowdhury R. In-plane mechanical behavior of tri-chiral and anti-trichiral auxetic cellular structures. Int. J. Mech. Sci. 2025; 289: 110054.

[27] Gomes RA, de Oliveira LA, Francisco MB, Gomes GF. Tubular auxetic structures: a review. Thin-Walled Struct. 2023; 188: 110850.

[28] Fernandez Corbaton I, Rockstuhl C, Ziemke P, et al. New twists of 3d chiral metamaterials. Adv. Mater. 2019; 31 (26): 1807742.

[29] Tobias, Frenzel, Muamer, Kadic, Martin, Wegene. Three-dimensional mechanical metamaterials with a twist. Science 2017; 358 (6366): 1072-4.

[30] Frenzel T, Köpfler J, Jung E, Kadic M, Wegener M. Ultrasound experiments on acoustical activity in chiral mechanical metamaterials. Nat. Commun. 2019; 10: 3384.

[31] Fleisch M, Thalhamer A, Meier G, et al. Asymmetric chiral and antichiral mechanical metamaterials with tunable poisson's ratio. APL Mater. 2022; 10 (6): 61105.

[32] Fleisch M, Thalhamer A, Meier G, et al. Chiral-based mechanical metamaterial with tunable normal-strain shear coupling effect. Eng Struct. 2023; 284: 115952.

[33] Wei Y, Yang Q, Tao R. Smp-based chiral auxetic mechanical metamaterial with tunable bandgap function. Int. J. Mech. Sci. 2021; 195: 106267.

[34] Zhao W, Zhu J, Liu L, Leng J, Liu Y. Analysis of small-scale topology and macroscale mechanical properties of shape memory chiral-lattice metamaterials. Compos. Struct. 2021; 262: 113569.

[35] Prall D, Lakes RS. Properties of a chiral honeycomb with a Poisson's ratio of — 1. Int. J. Mech. Sci. 1997; 39 (3): 305-7.

[36] Wojciechowski KW. Two-dimensional isotropic system with a negative poisson ratio. Phys. Lett. A 1989; 137 (1-2): 60-4.

[37] Alderson A, Alderson KL, Chirima G, Ravirala N, Zied KM. The in-plane linear elastic constants and out-of-plane bending of 3-coordinated ligament and cylinder-ligament honeycombs. Compos. Sci. Technol. 2010; 70 (7): 1034-41.

[38] Alderson A, Alderson KL, Attard D, et al. Elastic constants of 3-, 4- and 6-connected chiral and anti-chiral honeycombs subject to uniaxial in-plane loading. Compos. Sci. Technol. 2010; 70 (7): 1042-8.

[39] Jiang Y, Rudra B, Shim J, Li Y. Limiting strain for auxeticity under large compressive deformation: chiral vs. Re-entrant cellular solids. Int. J. Solids Struct. 2019; 162: 87-95.

[40] Grima JN, Gatt R, Farrugia PS. On the properties of auxetic meta-tetrachiral structures. Phys. Status Solidi 2010; 245 (3): 511-20.

[41] Mizzi L, Grasselli L, Spaggiari A. Clockwise vs anti-clockwise chiral metamaterials: influence of base tessellation symmetry and rotational direction of chiralisation on mechanical properties. Thin-Walled Struct. 2024; 205: 112381.

[42] Asakawa K, Hirano Y, Tan K, Ogasawara T. Bio-inspired study of stiffener arrangement in composite stiffened panels using a voronoi diagram as an indicator. Compos. Struct. 2024; 327: 117640.

[43] Li Z, Wu Z. A novel multiscale design method for porous structures with tunable anisotropy: varied-shape voronoi tessellation. Comput. Methods Appl. Mech. Eng. 2024; 432: 117378.

[44] Christodoulou I, Tan PJ. Crack initiation and fracture toughness of random voronoi honeycombs. Eng. Fract. Mech. 2013; 104: 140-61.

[45] Yuan Y, Zhang Y, Ruan D, et al. Deformation and failure of additively manufactured voronoi foams under dynamic compressive loadings. Eng. Struct. 2023; 284: 115954.

[46] Zhou Y, Isaksson P, Persson C. An improved trabecular bone model based on voronoi tessellation. J. Mech. Behav. Biomed. Mater. 2023; 148: 106172.

[47] Li Z, Chu S, Wu Z. A novel bio-inspired design method for porous structures: variable-periodic voronoi tessellation. Mater. Des. 2024; 243: 113055.

[48] Zou S, Gong H, Gao J. Study on design and impact energy absorption of voronoi porous structure with tunable Poisson's ratio. Thin-Walled Struct. 2024; 197: 111552.

[49] Zhang J, Wang Z, Zhao L. Dynamic response of functionally graded cellular materials based on the voronoi model. Composites, Part B 2016; 85: 176-87.

[50] Wang M, Zhang J, Lu G. A note on the modelling of foams using voronoi technique. Thin-Walled Struct. 2023; 187: 110745.

[51] Li K, Gao XL, Wang J. Dynamic crushing behavior of honeycomb structures with irregular cell shapes and non-uniform cell wall thickness. Int. J. Solids Struct. 2007; 44 (14-15): 5003-26.

[52] Ajdari A, Nayeb-Hashemi H, Canavan P, Warner G. Effect of defects on elastic–plastic behavior of cellular materials. Mater. Sci. Eng., A 2008; 487 (1-2): 558-67.

[53] Do QT, Nguyen CHP, Choi Y. Homogenization-based optimum design of additively manufactured voronoi cellular structures. Addit. Manuf. 2021; 45: 102057.

[54] Pham RD, Hütter G. Influence of topology and porosity on size effects in stripes

of cellular material with honeycomb structure under shear, tension and bending. Mech. Mater. 2021; 154: 103727.

[55] Colamartino I, Anghileri M, Boniardi M. Investigation of the compressive properties of three-dimensional voronoi reticula. Int. J. Solids Struct. 2023; 284: 112501.

[56] Hooshmand-Ahoor Z, Tarantino MG, Danas K. Mechanically-grown morphogenesis of voronoi-type materials: computer design, 3d-printing and experiments. Mech. Mater. 2022; 173: 104432.

[57] Schaffner G, Guo XE, Silva MJ, Gibson LJ. Modelling fatigue damage accumulation in two-dimensional voronoi honeycombs. Int. J. Mech Sci. 2000; 42 (4): 645-56.

[58] Choukir S, van Egmond DA, Hatton BD, Hibbard GD, Singh CV. The interplay between constituent material and architectural disorder in bioinspired honeycomb structures. Int. J. Eng. Sci. 2023; 188: 103863.

[59] Silva MJ, Hayes WC, Gibson LJ. The effects of non-periodic microstructure on the elastic properties of two-dimensional cellular solids. Int. J. Mech. Sci. 1995; 37 (11): 1161-77.

[60] Silva MJ, Gibson LJ. The effects of non-periodic microstructure and defects on the compressive strength of two-dimensional cellular solids. Int. J. Mech. Sci. 1997; 39 (5): 549-63.

[61] Zhu HX, Hobdell JR, Windle AH. Effects of cell irregularity on the elastic properties of 2d voronoi honeycombs. J. Mech. Phys. Solids 2001; 49 (4): 857-70.

[62] Zhu HX, Thorpe SM, Windle AH. The geometrical properties of irregular two-dimensional voronoi tessellations. Philos. Mag. A 2001; 81 (12): 2765-83.

[63] Sotomayor OE, Tippur HV. Role of cell regularity and relative density on elasto-plastic compression response of random honeycombs generated using voronoi diagrams. Int. J. Solids Struct. 2014; 51 (21–22): 3776-86.

[64] Zhu HX, Thorpe SM, Windle AH. The effect of cell irregularity on the high strain

compression of 2d voronoi honeycombs. Int J Solids Struct. 2006; 43 (5): 1061-78.

[65] Zheng Z, Yu J, Li J. Dynamic crushing of 2d cellular structures: a finite element study. Int. J. Impact Eng. 2005; 32 (1/4): 650-64.

[66] Abdullahi HS, Gao S. A novel multi-cell square tubal structure based on voronoi tessellation for enhanced crashworthiness. Thin-Walled Struct. 2020; 150: 106690.

[67] Wang S, Wang H, Ding Y, Yu F. Crushing behavior and deformation mechanism of randomly honeycomb cylindrical shell structure. Thin-Walled Struct. 2020; 151 (11): 106739.

[68] Ji X, Zhang Y, Jiang WZ, et al. Design, fabrication and mechanical properties of an auxetic cylindrical sandwich tube with improved energy absorption. Thin-Walled Struct. 2025; 210: 113036.

[69] Zheng X, Chen T, Guo X, Samitsu S, Watanabe I. Controllable inverse design of auxetic metamaterials using deep learning. Mater. Des. 2021; 211: 110178.

[70] Zhao M, Cui J, Chen L, Jin K, Zeng Z. Enhanced mechanical properties and energy absorption of lattice metamaterials inspired by crystal imperfections. Compos. Struct. 2025; 356: 118894.

[71] Yu P, Zhang P, Ji Q, et al. A multi-step auxetic metamaterial with instability regulation. Int. J. Solids Struct. 2024; 305: 113040.

[72] Meng Z, Liu M, Zhang Y, Chen CQ. Multi-step deformation mechanical metamaterials. J. Mech. Phys. Solids. 2020; 144: 104095.

[73] Meng Z, Ouyang Z, Chen CQ. Multi-step metamaterials with two phases of elastic and plastic deformation. Compos. Struct. 2021; 271: 114152.

[74] Wang S, Liu H. Quasi-static compression response of a novel multi-step auxetic honeycomb with tunable transition strain. Aerosp. Sci. Technol. 2024; 155: 109730.

[75] Wang X, Zou L, Cai C, et al. Energy absorption structure with negative stepped plateau force characteristics under quasi-static loads. Thin-Walled Struct. 2024; 205: 112506.

[76] Ma X, Zhang N, Zhang C, Tian X. Mechanical behavior of a novel lattice structure

with two-step deformation. Thin-Walled Struct. 2024; 197: 111580.

[77] Zhang W, Yan Z, Zhang J, et al. On in-plane crushing behavior of an improved double-arrow auxetic metamaterial with two-step deformation mode. Eng. Struct. 2024; 303: 117482.

[78] Guo S, Gao R, Tian X, Liu S. A quasi-zero-stiffness elastic metamaterial for energy absorption and shock attenuation. Eng. Struct. 2023; 280: 115687.